Medical Engineering and Physics 73 (2019) 64–72

Contents lists available at ScienceDirect

Medical Engineering and Physics

journal homepage: www.elsevier.com/locate/medengphy

Designing pre-tensioned core-shell fibers to treat pelvic floor disorders

Michael P.H. Lau[a,b], Leonard F. Pease III[a,c,*]

[a] Novo Contour, Inc., Edmonds WA 98026, USA
[b] Total Women's Health, Edmonds, WA 98026, USA
[c] Departments of Chemical Engineering, Internal Medicine and Pharmaceutics & Pharmaceutical Chemistry, University of Utah, Salt Lake City, UT 84112, USA

ARTICLE INFO

Article history:
Received 19 January 2019
Revised 19 May 2019
Accepted 7 July 2019

Keywords:
Surgical mesh and sutures
Delamination criteria
Soft connective tissue

ABSTRACT

Here we relate support provided to the pelvic floor by composite fibers having pre-tensioned cores secured by thin shells to tunable fiber properties. Surgical treatment of pelvic floor disorders including stress urinary incontinence and pelvic organ prolapse often inserts polymeric mesh to support pelvic fascia. However, achieving optimal levels of mesh tension and organ lift in minimally invasive surgeries remains challenging. Fibers with pre-tensioned cores and biodegradable shells have the potential to overcome this challenge by allowing reconstructive surgeons to "dial in" specific amounts of support without over tensioning mesh slings, which may lead to soft tissue erosion and voiding dysfunction. Consequently, this study quantifies the relationship between fiber dimensions and properties with the lift these fibers (once integrated into mesh) can provide to pelvic organs. Our linear elastic model quantifies the minimum and maximum amount of pre-tensioning allowed from tissue lift and core-shell delamination considerations, respectively. The model indicates that the elastic modulus of the biodegradable shell polymer should be orders of magnitude larger than that of the core polymer and be at least 10% of the core radius to preserve tension within the core that subsequently translates into tissue support.

1. Introduction

Surgical treatment for pelvic floor disorders involves the placement of either natural tissue or synthetic mesh to support pelvic organs to prevent prolapse (e.g., cystocele, rectocele, enterocele, and uterine prolapse) and stress urinary incontinence (SUI) [1–5]. For example in healthy patients, the urethrovesicle junction (UVJ), commonly called the bladder neck, is supported by a thin (~3 mm thick) layer of pelvic fascia [6–7]. When the fascia weakens or elongates over time or stretches due to childbirth, the UVJ falls from its preferred position superior to the base of the bladder during Valsalva's events, facilitating urinary incontinence [2,8–10]. To provide additional support, most gynecological surgeons use polymer mesh that, although they do not mimic the stress-strain curves of native tissue [11–12], are readily available, sterilized, and inserted as a suburethral sling on an outpatient basis [13–19]. (Although natural tissue may provide a better match to the mechanical properties of the patient's tissue, natural tissues remain in short supply.) However, properly tensioning commercially available mesh is challenging with state-of-the-art surgical techniques and materials.

Historically, treatment of incontinence and pelvic organ prolapse (POP) called for open surgery [9]. Surgical trainees learned to properly tension sutures and tissue to provide optimal benefit, because over tensioning leads to urethral stenosis, voiding dysfunction, urinary retention and increased risk of mesh erosion, while under tensioning renders the surgery ineffective [16,20–23]. Success rates for treatment of SUI by open surgery, such as retropubic urethroplexy, can exceed 97% but require extended recovery [9,17,19,24]. With the advent of minimally invasive surgical techniques, patient recovery is more rapid, but long-term success rates have been more modest and disparate ranging from <70% to 85%, in part because achieving optimal levels of tension is challenging in confined environments [9,17,19,24]. Recent studies show >30% of patients require two surgeries to correct incontinence [9,17,19,24], and the cure rates for cystocele remain as low as 37% [25]. Successful treatment often depends significantly on an individual surgeon's technique, leading to dramatic differences in success rates among centers [25]. The inability to readily achieve optimal levels of tension in confined spaces is a general problem affecting nearly all pelvic reconstructive surgeries.

Pre-tensioned core-shell fibers have the potential to overcome these limitations by allowing reconstructive surgeons to "dial in"

List of Abbreviations:: UVJ, urethrovesicle junction; POP, pelvic organ prolapse; SUI, stress urinary incontinence; FFT, Finite Fourier Transform; PDMS, poly(dimethyl siloxane); PLA, poly(lactic acid); ISD, intrinsic sphincter deficiency.

[*] Corresponding author at: Departments of Chemical Engineering, Internal Medicine and Pharmaceutics & Pharmaceutical Chemistry, University of Utah, Salt Lake City, UT 84112, USA.

E-mail address: pease@eng.utah.edu (L.F. Pease III).

https://doi.org/10.1016/j.medengphy.2019.07.004
1350-4533/

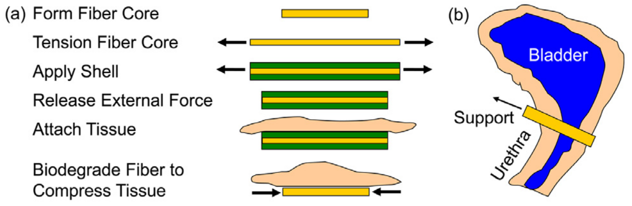

Fig. 1. (a) Pre-tensioned core-shell fiber preparation and degradation scheme. Applying a polymeric shell to a tensioned core locks it in place. Biodegradation of the shell releases the tension to contract adjacent tissue. (b) Support provided by the fibers in mesh lifts the female urethra to prevent urinary incontinence.

specific amounts of tension that can be released gradually to lift pelvic organ support structures, minimizing the temptation for surgeons to overtension mesh slings to achieve immediate surgical effect and decreasing the risk of tissue erosion and post-surgical voiding dysfunction [16,20–23]. Pre-tensioning of the fiber is achieved by stretching the fiber core to a predetermined length and then securing it in its elongated state by applying a shell coating (see Fig. 1). Biodegrading or bioeroding the shell *in vivo* then releases the tension as the fiber anchored within a mesh shrinks, gradually lifting the pelvic organs resting upon it in much the same way as degradation of enteric coatings enables timed release of pharmaceutical agents within the gastrointestinal tract. The gradual change in lift may allow local tissue remodeling to synchronize with innate healing mechanisms.

Although the above strategy is straightforward, a significant barrier to its implementation in clinical practice is the lack of a clear relationship between the lift and support these fibers provide to pelvic organs and the fiber dimensions and material properties. Here we address this barrier by determining the fiber properties necessary to provide a specific amount of lift to organs proximal to the pelvic floor. We generate and solve a mathematical model to relate the fiber geometry and material properties to fiber shrinkage, and then relate the shrinkage to the lift provided to pelvic organs. We conclude by discussing the implications of the design space for successful treatment of pelvic floor disorders.

2. Methods: model

Here the fibers forming the mesh are modeled as nominally straight with minimal to negligible curvature. Large polymer deformations may require consideration of hyperelasticity, but the deformations here are assumed to be sufficiently small so that selected polymers remain Hookian. Weaving, molding or other processes that combine the fibers into mesh remain beyond the scope of this article. In contrast to traditional mesh where only one polymer is selected for the entire mesh, each fiber is composed of at least two polymers and different fibers of different compositions and dimensions may be composed into the mesh. Therefore, a general model that explores fiber material properties and dimensions is explored below.

The equations of linear elasticity are used to model the stress transfer process in three distinct steps (see Fig. 1) [26–27]. First, a cylindrical fiber is stretched from an unstressed state to an applied strain of $u_{zz}{}^{co}$ (Fig. 2a). This strain is secured by coating the fiber with an unstressed polymeric shell. Second, the applied tension to the core is released, causing it to partially retract and the shell to partially compress (Fig. 2b). However, the core remains in tension because the shell resists compression via shear stresses at the core-shell interface. Tension remaining at the end of this step that is available to support the pelvic organs following reconstructive surgery, but excessive tension may also cause core-shell delamination. Third, the fibers are implanted as a mesh to support organ weight. The shell then biodegrades or bioerodes allowing the tension stored in the core to provide additional lift (Fig. 3cd). Organ weight along with fiber material properties determine the effective lift provided by the mesh and the minimum amount of pre-tensioning required.

2.1. Initial core tension

We consider a core-shell fiber with z oriented along the length of the fiber, r directed radially, and θ oriented azimuthally (see Fig. 2). A stress $\sigma_{zz}{}^o$ is applied to the fiber core to induce an increase in length of $u_{zz}{}^{co}$ and provide the initial tension. We adopt the notation given by Landau, et al., where duplicate subscripts denote normal stresses and strains [27–29]. The superscript "o" represents the initial stress applied to the fiber core. The shell of the fiber is then applied in a stress-free manner (e.g., dip coating). Because our system is considered to be axissymetric, angular strains and derivatives thereof remain vanishingly small. Using the isothermal equations of linear elasticity at steady state in the absence of bulk forces and reducing our domain to stresses below the yield stress (a limit to the effective amount of stress that can be applied), we determine the following initial stresses and strains in the fiber before it partially retracts [26–28,30]. Stresses are designated as σ_{ij} and strains as u_{ij} with subscripts designating coordinates. In both core and shell, $\sigma_{rr}{}^o = u_{rz}{}^o = u_{zr}{}^o = \sigma_{rz}{}^o = \sigma_{zr}{}^o = \sigma_{\theta\theta}{}^o = 0$, in the shell, $\sigma_{zz}{}^o = u_{zz}{}^o = u_{rr}{}^o = u_{\theta\theta}{}^o = 0$, and in the core, $\sigma_{zz}{}^o = E_c u_{zz}{}^{co}$,

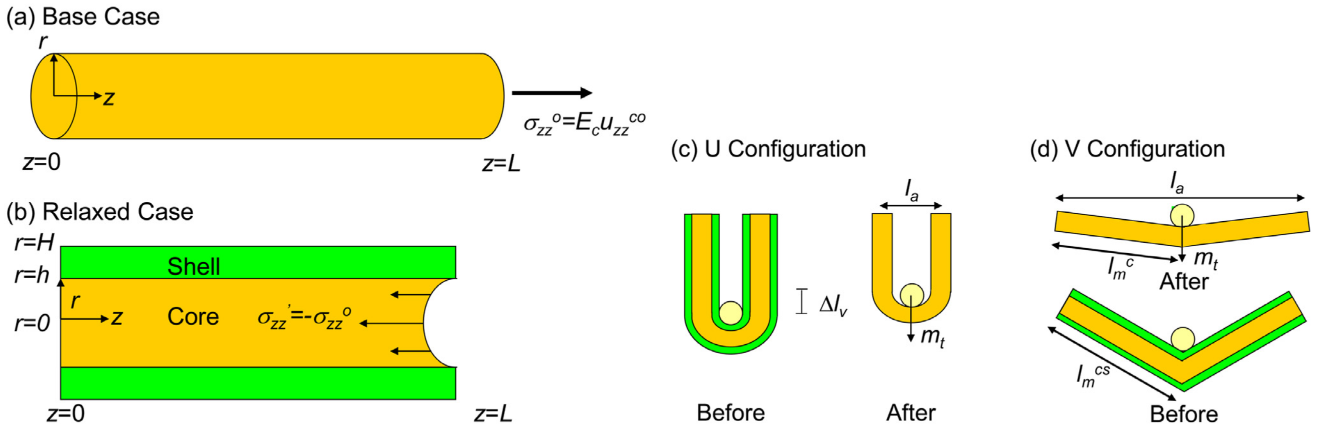

Fig. 2. Coordinate system and stresses for one half of a fiber for (a) base case (denoted by ^{o}) and (b) relaxed case (denoted by '). Mesh configurations lifting the UVJ (circle) in (c) a U configuration and (d) a V configuration. Each mesh comprises several fibers, one of which is shown in cross section. The organ mass (e.g., the UVJ) is m_t and the distance between ends of the mesh is l_a.

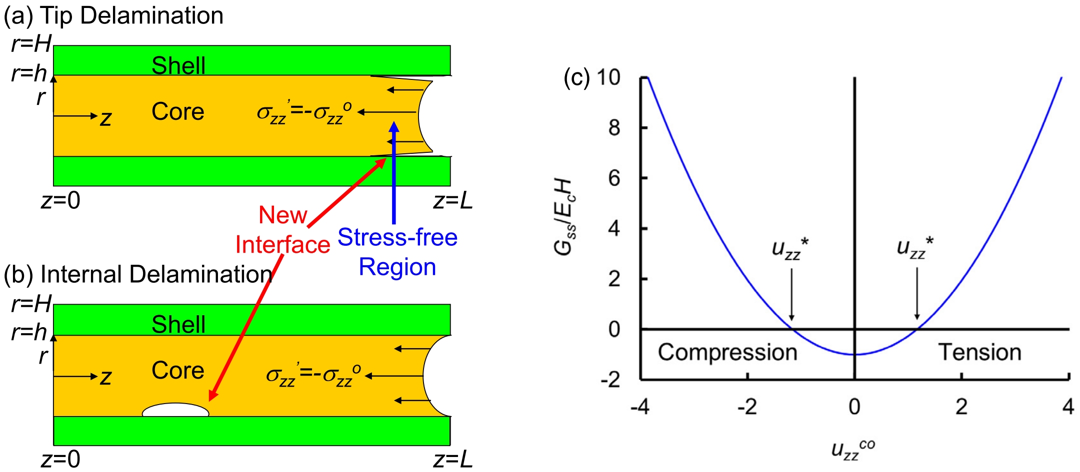

Fig. 3. Diagram of (a) tip and (b) internal delamination, showing that only tip delamination creates a stress-free region to drive delamination. The panel does not depict core expansion upon contraction that would self-limit delamination. (c) G_{ss}/E_cH versus $u_{zz}{}^{co}$ for $H/L = 0.01$, $\nu_c = 0.45$, $\nu_s = 0.33$, $\sigma_t/E_c = 0$, $E_c/E_s = 0.01$, $h/H = 0.9$, and $(\gamma_s + \gamma_c - \gamma_{sc})/(E_cH) = 1$. The two x-axis intercepts represent $u_{zz}{}^*$, and values of $u_{zz}{}^{co}$ between these two intercepts represent strains that do not cause delamination. The positive root is the delamination strain for pre-tensioned fibers, while the negative root is the delamination strain for pre-compressed fibers.

$u_{zz}{}^o = u_{zz}{}^{co}$, $u_{rr}{}^o = \text{-}\nu_c u_{zz}{}^{co}$, and $u_{\theta\theta}{}^o = \text{-}\nu_c u_{zz}{}^{co}$. The value $u_{zz}{}^{co}$ designates the initial strain in the core that provides a mathematical driving force. The elastic moduli in core and shell are E_c and E_s, respectively, while the Poisson's ratios in the core and shell are ν_c and ν_s. Cylindrical coordinates introduce a nonzero $u_{\theta\theta}{}^o$ even though $\sigma_{\theta\theta}{}^o$ remains zero throughout the remainder of the analysis.

2.2. After release of tension

When clamps tensioning the core are released, it partially retracts developing internal stresses in the absence of external surface forces acting on the fiber shell. The core remains held in tension by shear stresses from the shell, while the shell compresses as a result of shear stresses from the core. Linearity allows us to write

$$\sigma_{ij} = \sigma_{ij}{}^o + \sigma'_{ij} \tag{1a}$$

and

$$u_{ij} = u_{ij}{}^o + u'_{ij}, \tag{1b}$$

where the prime denotes the additional stress and strain fields developed after release of the external surface force acting on the core alone [28–30]. Steady-state conservation of momentum in the absence of bulk forces demands that

$$\frac{1}{r}\frac{\partial r\sigma_{zr}}{\partial r} + \frac{\partial \sigma_{zz}}{\partial z} = 0 \tag{2a}$$

and

$$\frac{1}{r}\frac{\partial r\sigma_{rr}}{\partial r} + \frac{\partial \sigma_{rz}}{\partial z} = 0 \tag{2b}$$

in the isotropic homogeneous media of the core and shell [26–28] with

$$\sigma_{rr} = \frac{E}{(1+\nu)(1-2\nu)}[(1-\nu)u_{rr} + \nu u_{zz} + \nu u_{\theta\theta}], \tag{3a}$$

$$\sigma_{rz} = \frac{E}{1+\nu}u_{rz}, \tag{3b}$$

$$\sigma_{zz} = \frac{E}{(1+\nu)(1-2\nu)}[(1-\nu)u_{zz} + \nu u_{rr} + \nu u_{\theta\theta}], \tag{3c}$$

$$\sigma_{zr} = \frac{E}{1+\nu}u_{zr}, \tag{3d}$$

$$u_{rr} = \frac{\partial u_r}{\partial r}, \tag{3e}$$

$$u_{zz} = \frac{\partial u_z}{\partial z}, \tag{3f}$$

and

$$u_{rz} = \frac{1}{2}\left(\frac{\partial u_r}{\partial z} + \frac{\partial u_z}{\partial r}\right), \tag{3g}$$

where u_z and u_r represent dimensional deformation in the axial and radial directions. We recognize that the initial core tension solutions (i.e., the base case) are independent of spatial coordinates and neglect the smaller radial and azimuthal deformation in the prime case to allow for partial decoupling of the equations and the use of separation-of-variables solutions [28–30].

The decoupled equations in the core are

$$\frac{1}{r}\frac{\partial}{\partial r}r\frac{\partial u_z{}'}{\partial r} + \frac{2(1-\nu_c)}{1-2\nu_c}\frac{\partial^2 u_z{}'}{\partial z^2} = 0, \tag{4a}$$

$$u_z{}' = 0 \qquad @z = 0, \tag{5a}$$

$$\frac{\partial u_z{}'}{\partial z} = \frac{(1+\nu_c)(1-2\nu_c)}{1-\nu_c}\left(\frac{\sigma_t}{E_c} - u_{zz}{}^{co}\right) \quad @z = L, \tag{6a}$$

$$\frac{\partial u_z{}'}{\partial r} = 0 \quad @r = 0, \tag{7a}$$

and

$$\frac{E_c}{1+\nu_c}\frac{\partial u_z{}'}{\partial r}\bigg|_{core} = \frac{E_s}{1+\nu_s}\frac{\partial u_z{}'}{\partial r}\bigg|_{shell} \quad @r = h, \tag{8a}$$

and in the shell

$$\frac{1}{r}\frac{\partial}{\partial r}r\frac{\partial u_z{}'}{\partial r} + \frac{2(1-\nu_s)}{1-2\nu_s}\frac{\partial^2 u_z{}'}{\partial z^2} = 0, \tag{4b}$$

$$u_z{}' = 0 \quad @z = 0, \tag{5b}$$

$$\frac{\partial u_z{}'}{\partial z} = \frac{(1+\nu_s)(1-2\nu_s)}{1-\nu_s}\frac{\sigma_t}{E_s} \quad @z = L, \tag{6b}$$

$$\frac{\partial u_z{}'}{\partial r} = 0 \quad @r = H, \tag{7b}$$

Table 1
Typical values of dimensionless groups.

Dimensionless group	Minimum value	Nominal value	Maximum value
H^2/L^2	0.000025	0.0001	1
ν_c	0.25	0.45	0.5
ν_s	0.25	0.33	0.5
$u_{zz}{}^{co}$	0	1	10
E_c/E_s	10^{-5}	0.01	1
h/H	0	0.9	1
$(\gamma_s+\gamma_c\text{-}\gamma_{sc})/(E_cH)$	10^{-5}	2	5
$(m_tg+F)/(2\pi NE_ch^2)$	10^{-4}	0.158	10^5
$(l_a/l_m{}^{co})^2$	0	0.6	1

*based approximately on $H=1$ mm, $L=10$ cm (1 mm to 20 cm), $\nu_c=0.45$, $\nu_s=0.33$, $u_{zz}{}^{co}=1$ (0 to 10), $E_c=1$ MPa (0.1–10 MPa), $E_s=100$ MPa (10–10^4 MPa), $h=0.9$ mm (0–1 mm), $(\gamma_s+\gamma_c\text{-}\gamma_{sc})=20$ J/m^2 (0.01–50 J/m^2), $N=10$ (5–100), $m_t=0.65$ kg (0.075–0.65 kg), $l_m{}^{co}=18$ cm (1 mm to 20 cm), and $l_a=14$ cm (1 mm to 20 cm).

and

$$u_z'|_{core}=u_z'|_{shell} \quad @r=h. \tag{8b}$$

The boundary conditions represent a fixed z axis at the center of the fiber, normal stress applied to the end of the fiber (at $z=L$) with applied load or stress σ_t, shear stresses on the center and sides of the fiber, and continuity boundary conditions at the core-shell interface, respectively. The fiber radius is H, the core radius is h, and the half length of the fiber is $L(=l_m{}^{co}(1+u_{zz}{}^{co})/2$, where $l_m{}^{co}$ is the initial length of the fiber prior to relaxation). Eqs. (6) provide the primary driving force, while Eqs. (8) couple together the core and shell displacement and shear.

These equations are scaled to reduce the number of parameters required without loss of rigor. Scaling generates a set of dimensionless ratios or dimensionless parameters to fully explore the parameter space using a minimal set of computations (see Table 1 for groups with representative values). We scale axial positions and displacements (u_z and z) on L and radial positions and displacements (u_r and r) on H, using overbars to denote scaled quantities. The scaled equations, reported in the Supplementary Material, are solved using a Finite Fourier Transform (FFT) [31]. FFT is the equivalent of separation of variables in the form of

$$\bar{u}_z(\bar{r},\bar{z})=\sum_{n=0}^{\infty}C_n(\bar{r})\varphi_n(\bar{z}), \tag{9}$$

where C_n is a spectral coefficient and ϕ_n is the basis function. The latter is chosen via the form of the boundary conditions with the mixed Neumann and Dirichlet conditions above to be

$$\varphi_n(\bar{z})=\sqrt{2}\mathrm{Sin}\left[\left(n+\tfrac{1}{2}\right)\pi\bar{z}\right] \tag{10}$$

for $n=0$, 1, 2... This basis function was chosen to be a function of z to avoid issues arising from discontinuities in shear displacement along the core-shell interface [31]. Multiplying $\bar{u}_z(\bar{r},\bar{z})$ by the basis function and integrating with respect to $\bar{z}$ from zero to unity defines

$$\theta_n(\bar{r})\equiv\int_{\bar{z}=0}^{\bar{z}=1}\bar{u}_z(\bar{r},\bar{z})\varphi_n(\bar{z})d\bar{z}. \tag{11}$$

As shown in the Supplementary Material, transformation and integration yields

$$\theta_n{}^c=-\frac{A_1}{A_2{}^2}+c_1I_o(A_2\bar{r}) \tag{12a}$$

and

$$\theta_n{}^s=c_3I_o(A_4\bar{r})+c_4K_o(A_4\bar{r})+\frac{A_3}{A_4{}^2}, \tag{12b}$$

in terms of modified Bessel functions of the first and second kinds, I_ν and K_ν of order ν, respectively, with constants

$$A_1=2\sqrt{2}(-1)^n\frac{H^2}{L^2}(1+\nu_c)\left(u_{zz}{}^{co}-\frac{\sigma_t}{E_c}\right), \tag{13a}$$

$$A_2=\sqrt{\frac{H^2}{L^2}\frac{2(1-\nu_c)}{1-2\nu_c}\left(n+\tfrac{1}{2}\right)^2\pi^2}, \tag{13b}$$

$$A_3=2\sqrt{2}(-1)^n\frac{H^2}{L^2}(1+\nu_s)\frac{\sigma_t}{E_s}, \tag{13c}$$

and

$$A_4=\sqrt{\frac{H^2}{L^2}\frac{2(1-\nu_s)}{1-2\nu_s}\left(n+\tfrac{1}{2}\right)^2\pi^2} \tag{13d}$$

with constants c_1-c_4 given in the Supplementary Material. Deen [31] shows that $\theta_n=C_n$, such that our final solution is given piecewise as

$$\bar{u}_z(\bar{r},\bar{z})=\begin{cases}\sum\limits_{n=0}^{\infty}\theta_n{}^c(\bar{r})\phi_n(\bar{z}) & for \quad \bar{r}\le\bar{h}\\ \sum\limits_{n=0}^{\infty}\theta_n{}^s(\bar{r})\phi_n(\bar{z}) & for \quad \bar{r}>\bar{h},\end{cases} \tag{14}$$

where superscripts c and s indicate the core and shell respectively. This value of $\bar{u}_z(\bar{r},\bar{z})$ represents the displacement after release of the applied tension. Notably, negative values of $\bar{u}_z(\bar{r},\bar{z})$ are appropriate in each case, because this value represents retraction, with more negative values in the core as reported below. Fig. S1 in the Supplementary Material shows these series converge with sufficient rapidity.

2.3. Delamination

Delamination may occur either at the tip or within the interior (see Fig. 3ab). However, if delamination occurs in the interior, the core cannot retract and the shell cannot extend to decrease the magnitude of their stress fields, severely limiting elastic energy recovery that would drive delamination [26,29–30,32]. Therefore, our analysis focuses on delamination from the tip inward, whence the core can partially retract and the shell can partially expand to relieve stress. If the energy associated with stress relaxation exceeds the amount of energy required to form the new surface then the delamination will propagate. Following the pattern given by Griffiths, we consider a unit area of new crack [26,29–30,32]. Its new surface energy is

$$\Delta SE=2\pi hL(\gamma_s+\gamma_c-\gamma_{cs}), \tag{15}$$

where γ_s is the shell-air surface energy, γ_c is the core-air surface energy, and γ_{cs} is the core-shell interfacial energy. The interfacial energy can be approximated to first order by $\gamma_{cs}=(\gamma_c\gamma_s)^{1/2}$ [33]. The product $\sigma_{ij}u_{ij}$ represents the elastic energy per unit volume. Integrating over the volume of both parts of the fiber gives the elastic energy as

$$\begin{aligned}\Delta EE&=\int_0^{2\pi}\int_0^h\int_0^L\left(\sigma_{ij}{}^o+\sigma_{ij}{}'\right)\left(u_{ij}{}^o+u_{ij}{}'\right)dzrdrd\theta\\&\quad+\int_0^{2\pi}\int_h^H\int_0^L\left(\sigma_{ij}{}'\right)\left(u_{ij}{}'\right)dzrdrd\theta,\end{aligned} \tag{16}$$

where the first and second terms represent the energy of the core and shell before stress relaxation from delamination, respectively. The elastic energy after relaxation is zero because the core and shell are assumed to be stress free. Therefore, the total energy change from before to after crack formation is given as

$$\begin{aligned}\Delta E&=-\int_0^{2\pi}\int_0^h\int_0^L\left(\sigma_{ij}{}^o+\sigma_{ij}{}'\right)\left(u_{ij}{}^o+u_{ij}{}'\right)dzrdrd\theta\\&\quad-\int_0^{2\pi}\int_h^H\int_0^L\left(\sigma_{ij}{}'\right)\left(u_{ij}{}'\right)dzrdrd\theta+2\pi hL(\gamma_s+\gamma_c-\gamma_{cs}).\end{aligned} \tag{17}$$

When ΔE falls below zero, the crack may propagate. This expression may be written in terms of the steady-state energy release rate often reported in the literature on fracture in cylindrical coordinates as $G_{ss} \equiv -\Delta E/2\pi hL$ [26,30,32]. Substitution and scaling then yield

$$\begin{aligned}\frac{G_{ss}}{E_cH} = {} & \frac{1}{2}u_{zz}{}^{co2}\bar{h} + \frac{2-2\nu_c-3\nu_c{}^2}{(1+\nu_c)(1-2\nu_c)}\frac{u_{zz}{}^{co}}{\bar{h}}\sum_{n=0}^{\infty}\sqrt{2}(-1)^n\int_0^{\bar{h}}\theta_n{}^c(\bar{r})\bar{r}d\bar{r} \\ & - \frac{\gamma_s+\gamma_c-\gamma_{cs}}{E_cH} \\ & + \frac{(1-\nu_c)\pi^2}{\bar{h}(1+\nu_c)(1-2\nu_c)}\sum_{n=0}^{\infty}\left(n+\frac{1}{2}\right)^2\int_0^{\bar{h}}\theta_n{}^c(\bar{r})^2\bar{r}d\bar{r} \\ & + \frac{E_s}{E_c}\frac{(1-\nu_s)\pi^2}{\bar{h}(1+\nu_s)(1-2\nu_s)}\sum_{n=0}^{\infty}\left(n+\frac{1}{2}\right)^2\int_{\bar{h}}^{1}\theta_n{}^s(\bar{r})^2\bar{r}d\bar{r}. \end{aligned} \quad (18)$$

The maximum initial strain, $u_{zz}{}^*$, the fiber can sustain without delaminating can be determined from the first law of thermodynamics by setting $G_{ss} \equiv 0$ leaving $u_{zz}{}^* = u_{zz}{}^{co}$, which has two solutions as shown in Fig. 3c [30,32]. The positive root corresponds to delamination from pre-tensioning.

2.4. Tissue lift after shell removal

The model above applies to individual fibers. We now consider a mesh composed of N fibers that stretch from anchor to anchor that directly oppose the organ applied force. We recognize that more elaborate lift models may be appropriate for more intricate mesh designs. Though these more elaborate models may be outside the scope of this article, the conceptual model presented should be considered a first-order approximation to inform prototype development and suggest possibilities. After the shell has biodegraded or bioeroded, tension stored in the core must lift the pelvic organs. We now determine how much lift a mesh composed of N fibers will provide as a function of material properties, initial strain, and organ weight. The mesh with length $l_m{}^{cs}$ (determined by the shell after pre-tensioning and relaxation as $l_m{}^{cs} = l_m{}^{co}(1+u_{zz}{}^{co})(1+\bar{u}_z)$, where $l_m{}^{co}$ represents the initial length of the mesh cores) is inserted without tensioning (i.e., is neither slack nor supports a load such that $\sigma_t = 0$ in Eqs. (6) and is anchored between points separated by a linear distance of l_a (e.g., between the so called white lines). When the shell degrades, the core of the fiber supports a point source load of $m_tg + F$ acting at the ends of the fiber mesh, where m_t is the mass associated with tissue, F represents other forces including Valsalva's events, and g is the gravitational constant. A force balance perpendicular to the line connecting the anchor points gives the final mesh length, $l_m{}^c$, composed of only cores after the shell has degraded as

$$m_tg + F = 2\pi h^2NE_c\left(l_m{}^c/l_m{}^{co} - 1\right)\mathrm{Cos}\theta, \quad (19)$$

where the angle θ is defined by $\mathrm{Sin}\theta = l_a/l_m{}^c$. This can be rearranged as

$$\frac{m_tg+F}{2\pi NE_ch^2} = \sqrt{1-\left(\frac{l_a}{l_m{}^{co}}\right)^2\left(\frac{l_m{}^{co}}{l_m{}^c}\right)^2}\left(\frac{l_m{}^c}{l_m{}^{co}}-1\right). \quad (20)$$

The term on the left gives our final dimensionless number, which represents the ratio of the stress applied by the tissue to the elastic modulus of the core. The vertical lift, Δl_v, provided by the freed cores is then

$$\frac{\Delta l_v}{l_m{}^{co}} = \frac{1}{2}\left(\sqrt{\left(\frac{l_m{}^{cs}}{l_m{}^{co}}\right)^2-\left(\frac{l_a}{l_m{}^{co}}\right)^2}-\sqrt{\left(\frac{l_m{}^c}{l_m{}^{co}}\right)^2-\left(\frac{l_a}{l_m{}^{co}}\right)^2}\right), \quad (21)$$

where $l_m{}^c$ is the length of the cores after the shells have degraded in contrast to $l_m{}^{cs}$ for which the shells remain. Eqs. (20)–(21) represent a complete set.

We now consider a limiting case. Surgeons may place the mesh in approximately either a U shape, such that the two arms of the mesh are nearly parallel, or a V shape, where the two arms of the mesh form a shallow V with respect to each other. The U case (where $\mathrm{Cos}\theta = 1$) is particularly simple and insightful. Where $l_a << l_m{}^{co} < l_m{}^{cs}$,

$$\frac{l_m{}^c}{l_m{}^{co}} = 1 + \frac{m_tg+F}{2\pi NE_ch^2}, \quad (22)$$

and the lift becomes

$$\frac{\Delta l_v}{l_m{}^{co}} = \frac{1}{2}\left(u_{zz}{}^{co} + \bar{u}_z + u_{zz}{}^{co}\bar{u}_z - \frac{m_tg+F}{2\pi NE_ch^2}\right). \quad (23)$$

The $u_{zz}{}^{co}\bar{u}_z$ product appears due to our selection of scales. This equation shows that to achieve lift, the pre-tensioning must be large enough to oppose both the initial retraction and the organ weight all without delaminating.

3. Results

The model predicts the fiber length immediately before surgical insertion relative to the initial core length to be given by $l_m{}^{cs}/l_m{}^{co} = (1+u_{zz}{}^{co})(1+\bar{u}_z)$, the maximum strain that can be applied before delamination is given by $u_{zz}{}^*$, and the amount of lift is given by $\Delta l_v/l_m{}^{co}$. The remainder of this analysis will determine how these depend on the dimensionless parameters summarized in Table 1. These parameters include three length scale ratios, namely, a diameter-to-length ratio, H^2/L^2; a dimensionless radial thickness of the core, $\bar{h} = h/H$; and a ratio of the distance between anchor points to the initial length of the mesh cores, $(l_a/l_m{}^{co})^2$. Other parameters include Poisson's ratios for the core and shell, ν_c and ν_s; the pre-tensioning strain, $u_{zz}{}^{co}$; the ratio of forces acting on the mesh to the elastic modulus and area of the core, $(m_tg+F)/(2\pi NE_ch^2)$; the ratio of elastic moduli of core to shell, E_c/E_s; and the ratio of surface energy to elastic energy, $(\gamma_s+\gamma_c\text{-}\gamma_{sc})/(E_cH)$.

Fig. 4 evaluates the relationship between the preinsertion fiber length (i.e., before removal of the shell) and these parameters. Fig. 4a shows the deformation profile at the fiber tip. The center of the core experiences most of the deformation or retraction as anticipated in Fig. 2b, because the shell resists core deformation. For typical initial strains, $u_{zz}{}^{co}$, the shell deforms only modestly but compresses significantly as the initial strain, $u_{zz}{}^{co}$ increases. Fig. 4b shows the relative thickness of the shell to be very influential. Each fiber retracts only modestly until the core exceeds 90% of the fiber diameter, at which point the deformation increases sharply until the fiber retracts completely to its initial prestrained position.

The remainder of Fig. 4 evaluates the role of the fiber elastic properties. Fig. 4c shows that while the elastic modulus of the shell is two orders of magnitude greater than the modulus of the core, the deformation is fairly modest, but as the two moduli approach parity, the shell cannot resist the shear stress imparted by the core. Therefore, the material with the larger elastic modulus must remain on the exterior of the fiber to retain the core tension for subsequent release. Fig. 4d shows that the Poisson's ratios only modestly affect deformation, except when either material becomes rubbery (i.e., where ν_c or ν_s approach ½). Indeed, Poisson's ratios of ½ can be used to prevent deformation even when E_c/E_s increases passed unity (see Fig. S3b).

The model also conservatively predicts when delamination may become problematic as seen in Fig. 5. Regions above the curves for $u_{zz}{}^*$ correspond to delaminating conditions, while those below are not predicted to delaminate by the model. The figure shows that

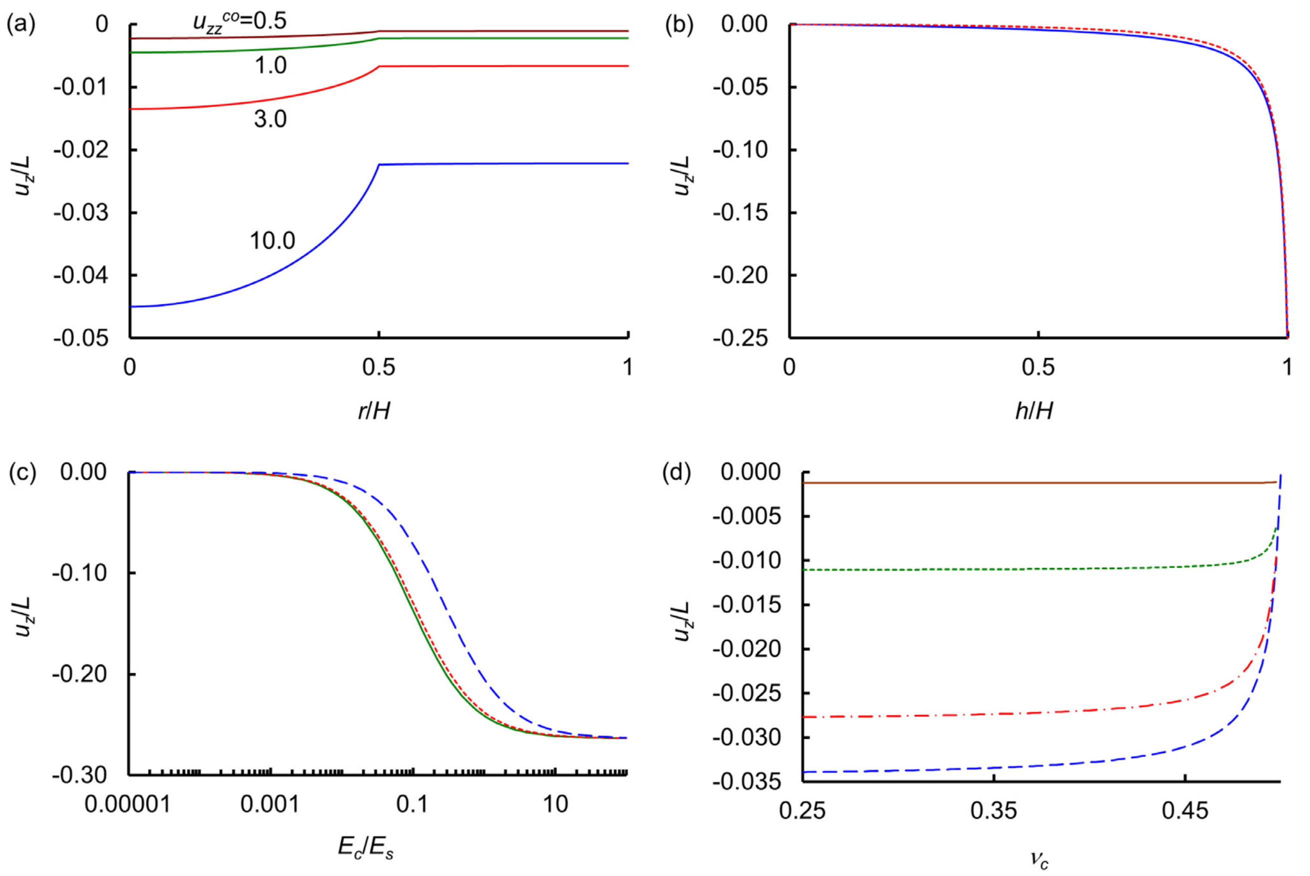

Fig. 4. (a) Relative fiber tip deformation, $u_z/L(r/H,1)$, versus fractional radius, r/H, for $u_{zz}^{co}=0.5$, 1, 3, and 10 with $h/H=0.5$, $H/L=0.01$, $\nu_c=0.45$, $\nu_s=0.33$, $E_c/E_s=0.01$, and $\sigma_t/E_c=0$. (b) Deformation at the fiber center, $u_z/L(0,1)$ (solid), and of the shell, $u_z/L(h/H$ to 1,1) (dash), versus relative core diameter, h/H, with $u_{zz}^{co}=1$, $H/L=0.01$, $\nu_c=0.45$, $\nu_s=0.33$, $E_c/E_s=0.01$, and $\sigma_t/E_c=0$. (c) Shell deformation, $u_z/L(h/H,1)$, versus E_c/E_s for $H/L=0.01$ (solid), 0.1 (short dash), and 1 (long dash) with $u_{zz}^{co}=1$, $\nu_c=0.45$, $\nu_s=0.33$, $h/H=0.9$, and $\sigma_t/E_c=0$. (d) Shell deformation, $u_z/L(h/H,1)$, versus ν_c for $\nu_s=0.25$ (long dash), 0.33 (alternating dash), 0.45 (short dash), and 0.495 (solid) with $h/H=0.9$, $H/L=0.01$, $u_{zz}^{co}=1$, $E_c/E_s=0.01$, and $\sigma_t/E_c=0$.

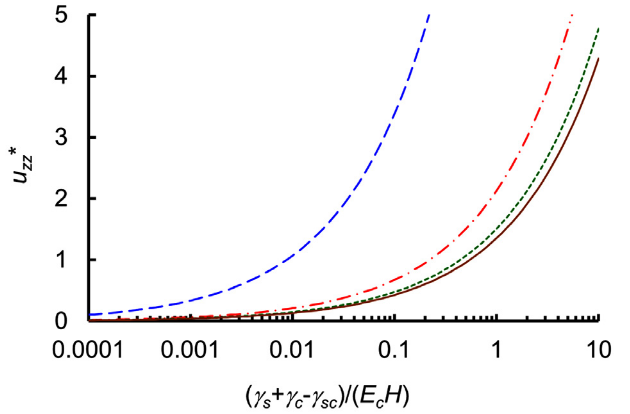

Fig. 5. The critical delamination stress, u_{zz}^*, versus $(\gamma_s+\gamma_c-\gamma_{sc})/(E_cH)$ for $h/H=0.01$ (long dash), 0.25 (alternating dash), 0.5 (short dash) and 0.99 (solid), $H/L=0.01$, $\nu_c=0.45$, $\nu_s=0.33$, and $E_c/E_s=0.01$.

thicker shells (smaller h/H) allow larger pre-strains. The figure also indicates that $(\gamma_s+\gamma_c-\gamma_{sc})/(E_cH)$ must be at least 0.01 to allow the core length to double ($u_{zz}^*=1$) without delamination, for example, though clinical deformations are expected to be much more modest as described below. To achieve doubling, E_c should be fairly modest and perhaps elastin like (e.g., $E_c<1.0$ MPa) and H should also be on the smaller end of the feasible range (between 10 nm and 1 mm). However, smaller diameter fibers would be required to sustain the same total organ load. The alternative is to adjust the surface energy that would be created by delamination. Interfacial energies range over several orders of magnitude reflecting numerous phenomena including van der Waals forces (0.01–0.05 J/m^2) [33–34], cleavage of chemical carbon-carbon bonds (0.4–1.2 J/m^2) [35], and also other lumped effects including local plasticity. Fracture data from Strobl inclusive of plasticity effects for polystyrene suggests values of 34.3–49.7 J/m^2 [36]. Thus, interfacial energies span a range exceeding three orders of magnitude, and the exact interfacial energies for a particular polymer system cannot be determined *a priori* due to the lack of comprehensive tables in the literature but must be measured experimentally for each polymer under consideration at the temperature of use. See Supplementary Material for additional results.

Finally, Fig. 6 shows that the lift, Δl_v, provided by the fibers depends strongly on $(m_tg+F)/(2\pi NE_ch^2)$ and u_{zz}^{co}. Only when $(m_tg+F)/(2\pi NE_ch^2)<1$ does a mesh composed of N fibers provide lift to the tissue (see Fig. 6a). Because the tissue weight is set by physiological constraints and varies from patient to patient, any one of three fiber parameters can be used to optimize surgical practice including the elastic modulus of the core, the diameter of the fiber core, and the number of fibers. Each of these variables individually contributes to the strength of the mesh and any of the three can be optimized in practice. This panel also shows a shallow V configuration with fibers extending linearly from anchor to anchor provides more lift at small masses because the cores must retract completely to the anchor-to-anchor length. Fig. 6b shows that as u_{zz}^{co} increases, the amount of lift increases proportionately for $u_{zz}^{co}<1$. The remaining parameters plotted in Fig. 6 play only a

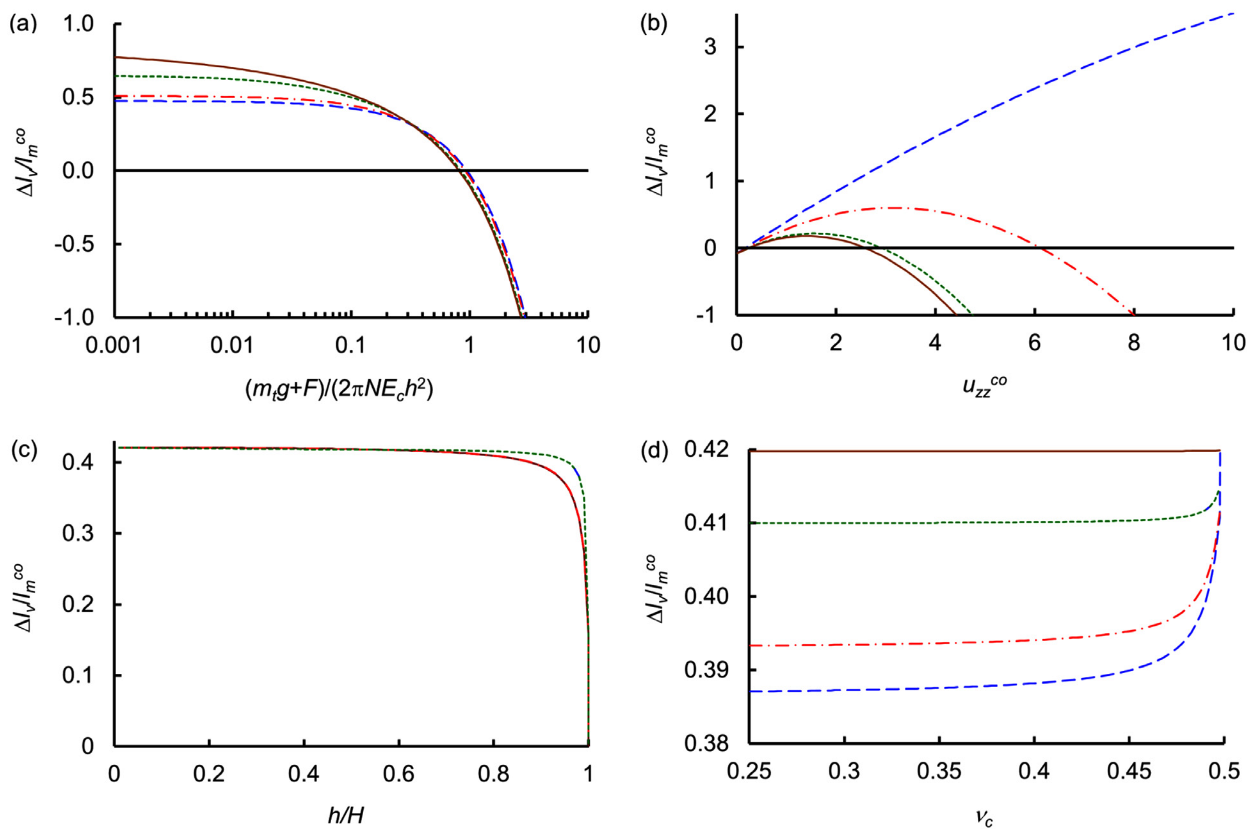

Fig. 6. (a) Relative lift, $\Delta l_v/l_m{}^{co}$, versus scaled force, $(m_t g+F)/(2\pi N E_c h^2)$, with $l_a/l_m{}^{co}=0.0$ (long dash), 0.5 (alternating dash), 0.9 (short dash), and 1.0 (solid) for $H/L=0.01$, $\nu_c=0.45$, $\nu_s=0.33$, $u_{zz}{}^{co}=1$, $E_c/E_s=0.01$, and $r/H=h/H=0.9$ at fiber tip. (b) Relative lift, $\Delta l_v/l_m{}^{co}$, versus pre-strain, $u_{zz}{}^{co}$, for $E_c/E_s=0.01$ (long dash), 0.1 (alternating dash), 1 (short dash), and 10 (solid) for $H/L=0.01$, $\nu_c=0.45$, $\nu_s=0.33$, $l_a/l_m{}^{co}=0$, $(m_t g+F)/(2\pi N E_c h^2)=0.158$, and $r/H=h/H=0.9$ at fiber tip. (c) Relative lift, $\Delta l_v/l_m{}^{co}$, versus relative fiber diameter, h/H $(=r/H)$, for $H/L=0.0001$ (solid), 0.01 (alternating dash), and 1 (long dash) for $\nu_c=0.45$, $\nu_s=0.33$, $E_c/E_s=0.01$, $u_{zz}{}^{co}=1$, $l_a/l_m{}^{co}=0$, and $(m_t g+F)/(2\pi N E_c h^2)=0.158$ at fiber tip. (d) Relative lift, $\Delta l_v/l_m{}^{co}$, versus core Poisson's ratio, ν_c, for $\nu_s=0.25$ (long dash), 0.33 (alternating dash), 0.45 (short dash), and 0.495 (solid) for $H/L=0.01$, $u_{zz}{}^{co}=1$, $E_c/E_s=0.01$, $r/H=h/H=0.9$, $l_a/l_m{}^{co}=0$, and $(m_t g+F)/(2\pi N E_c h^2)=0.158$ at fiber tip.

minor role in the amount of lift provided. So long as h/H remains less than 0.9, it does not affect the lift (though the lift falls off sharply as h/H approaches unity). Fig. 6d shows that more rubbery materials increase the amount of lift. Yet, these parameters only impact the amount of lift at the margins.

4. Discussion

This study considers the parameters needed to design pre-tensioned core-shell fibers that provide sufficient lift to support organ weight (supplementing native fascia where present) and counter balance the episodic downward force generated during Valsalva's events without delaminating. Polymer selection is critical and this analysis provides insight into selection tradeoffs. Our analysis finds that the polymer comprising the core should have a substantially lower elastic modulus than the shell polymer, because only tension preserved by the shell is available to support the tissue. For example, if the core were made of poly(dimethyl siloxane) (PDMS) with an elastin-like elastic modulus (e.g., <1.0 MPa), then selecting a collagen-like polymer such as poly(lactic acid) (PLA) with a substantially higher elastic modulus (e.g., >100 MPa) is important to keeping the core in tension prior to mesh implantation. Both polymers must be compatible with the adjacent tissue, and the shell polymer must be able to degrade on reasonable time scales.

The second critical design aspect is selection of the core pre-strain. Delamination serves as the upper limit to the amount of pre-strain allowed. Our analysis suggests that the elastomeric core may stretch to double its initial length ($u_{zz}{}^{co}=1$) for some conditions, provided the polymers remain linearly elastic. This is not a significant limitation because many elastomers double or triple their length without yielding significantly, many polymers may double in length before hyperelastic effects become important, and elastomers of clinical relevance can gain at least 50% of their initial length before yielding. This suggests that the amount of lift may be limited to less than the initial length of the core, but typical surgeries require changes on the order of millimeters whereas the length of the mesh is typically on the order of several centimeters. Indeed, Fig. 7 considers a typical case of only 17% strain, and target postoperative mesh contraction is likely modest (e.g., at most ~15%) [37]. Remarkably, pre-tensioning the core also inherently inhibits delamination. As the tension is released, the core expands as required by the Poisson's ratio, which in turn decreases any gap between the core and shell effectively hindering crack propagation. Therefore, one of the key advantages of the pre-tensioning approach is that delamination requires a higher initial stress than calculated herein. (We note in passing that the formalism developed herein may provide an innovative means of estimating the interfacial energy by measuring the stress at which core-shell fiber delamination occurs.)

Third, the physical dimensions of the fiber (i.e., the core radius and shell thickness) are also critical design parameters. The combination must remain less than ~3 mm characteristic of typical mesh and bandages. The model suggests that the shell thickness should be at least 10% of the core radius to preserve tension within the core that subsequently translates into tissue support.

Two additional factors affect the lift provided to the tissue. The first is the weight of the organ or tissue to be supported or the

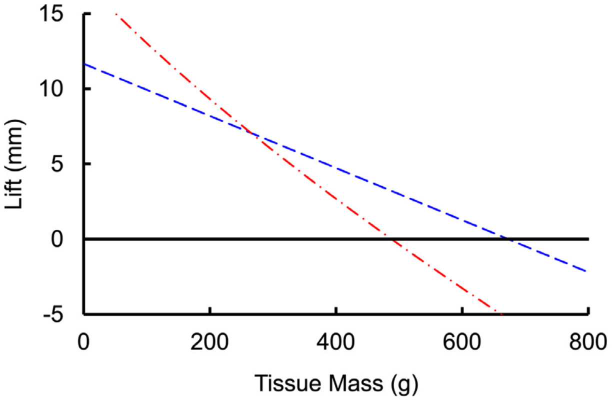

Fig. 7. Lift as a function tissue mass for a mesh with $N=25$ fibers, $E_c=0.4\,\text{MPa}$, $E_s=400\,\text{MPa}$, $l_m{}^{co}=18\,\text{cm}$, $L=l_m{}^{co}(1+u_{zz}{}^{co})/2=10.17\,\text{cm}$, $g=9.8\,\text{m/s}^2$, $h=0.90\,\text{mm}$, $\nu_c=0.45$, $\nu_s=0.33$, $H=1\,\text{mm}$, $u_{zz}{}^{co}=0.13$, and $F=0$ for U (long dash, $l_a=0$) and V (alternating dash, $l_a=14\,\text{cm}$) configurations.

force necessary to counter balance the episodic downward acceleration of Valsalva's events. Fig. 7 shows the amount of lift anticipated in absolute lengths for a PLA mesh with pre-tensioned PDMS cores with a pre-strain of 0.13 for both U and V configurations as a function of organ weight. In this first-order approximation and example, 25 fibers extend from anchor to anchor to provide support. As the weight increases (e.g., as the bladder fills), the lift decreases until the mesh provides no support when the tissue weight exceeds the tension stored in the mesh. The mass of the full bladder is approximately 400 g, suggesting that a lift of approximately 4.9 mm and 2.9 mm for the U and V configurations for these conditions, respectively. Please note that these deformations are rather small compared to the ~20 cm length of the fiber (i.e., <3%), supporting the modeling assertion of a linear elasticity. Although the preferred configuration depends on individual patient need, surgeons often prefer U shape slings (comprising mesh with anchors) to V shape ones to apply more pressure to the target tissue. For example, to treat intrinsic sphincter deficiency (ISD), applying a high pressure using a sub-urethral sling in a U configuration is preferable to press on the urethra to prevent SUI.

Although not a key element of the model presented here, an advantage of these mesh is their potential to apply tension to adjacent tissue gradually over time. By tuning the fiber dimensions, specifically the shell thickness, the tension release rate can in principle be precisely controlled. A thicker shell implies a longer degradation time. Because significant changes in fiber length occur when the shell is ≤10% of the fiber thickness, mesh design can incorporate a delay in tension release (i.e., a fuse) by making the shell thickness greater than 10% of the fiber radius. For surface eroding polymers that degrade steadily, the contraction will be predictable and gradual but increase steadily as the shell thins linearly, whereas bulk eroding polymers lead to less predictable changes in the shell thickness and hence the rate of lift. A complete understanding of these effects lies beyond the scope of this article. Nevertheless, by combining fibers of different dimensions, the overall tension release rate of the entire surgical mesh may be tuned, and multishell systems may counter any rapid jumps in tension. This is important because gradually tensioning the mesh as they integrate with the adjacent tissue allows cellular accommodation of the change in tension at a pace that is similar to intrinsic wound healing rather than sudden overtensioning at the time of state-of-the-art surgeries. Indeed, the mechanism used by fibroblasts remodel the matrix depends strongly on the mechanical loading (tension) of adjacent media and substrates [38].

In conclusion, this modeling effort indicates the feasibility of using pre-tensioned core-shell fibers to tunably lift pelvic organs. The model indicates that the elastic modulus of the biodegradable shell polymer should be orders of magnitude larger than that of the core polymer and be at least 10% of the core radius to preserve tension within the core that subsequently translates into tissue support.

Acknowledgements

The authors gratefully acknowledge helpful discussions with Ian C. McPhee and Benjamin J. Robinson. The authors acknowledge partial financial support from Novo Contour and the US National Institutes of Health NIA (R43AG039929-01). Neither significantly influenced the design or execution of this study.

Conflict of interest disclosure

The authors disclose previous partial ownership of Novo Contour and associated intellectual property. The authors disclose partial grant support as disclosed above.

Ethical approval

Not required.

Supplementary materials

Supplementary material associated with this article can be found, in the online version, at doi:10.1016/j.medengphy.2019.07.004.

References

[1] DeLancy JOL. The anatomy of the pelvic floor. Current Opin Obstet Gynecol 1994;6:313–16.
[2] Fielding JR. Practical MR imaging of female pelvic floor weakness. Radiographics 2002;22:295–304. doi:10.1148/radiographics.22.2.G02mr25295.
[3] Burgio KL, Matthews KA, Engel BT. Prevalence, incidence and correlates of urinary incontinence in healthy, middle-aged women. J Urol 1991;146:1255–9. doi:10.1016/s0022-5347(17)38063-1.
[4] Thom DH, Haan MN, Van Den Eeden SK. Medically recognized urinary incontinence and risks of hospitalization, nursing home admission and mortality. Age Ageing 1997;26:367–74. doi:10.1093/ageing/26.5.367.
[5] Waetjen LE, Liao S, Johnson WO, Sampselle CM, Sternfield B, Harlow SD, Gold EB. Factors associated with prevalent and incident urinary incontinence in a cohort of midlife women: a longitudinal analysis of data: study of women's health across the nation. Am J Epidemiol 2007;165:309–18. doi:10.1093/aje/kwk018.
[6] Hersh PS. Optics of conductive keratoplasty: implications for presbyopia management. Trans Am Ophthalmol Soc 2005;103:412–56. doi:10.1016/j.ajo.2006.06.025.
[7] Mostwin JL, Genadry R, Sanders R, Yang A. Anatomic goals in the correction of female stress urinary incontinence. J Endourol 1996;10:207–12. doi:10.1089/end.1996.10.207.
[8] Van Dongen L. The anatomy of genital prolapse. South African Medical Journal 1981;60:357–9.
[9] Raz S. Female urology. Phildelphia: W.B. Saunders Company; 1983.
[10] Dillon B, Dmochowski R. Radiofrequency for the treatment of stress urinary incontinence in women. Curr Urol Rep 2009;10:369–74. doi:10.1007/s11934-009-0058-z.
[11] Rubod C, Brieu M, Cosson M, Rivaux G, Clay J-C, de Landsheere L, Gabriel B. Biomechanical properties of human pelvic organs. Urology 2012;79:968.e17–968.e22. doi:10.1016/j.urology.2011.11.010.
[12] Martins P, Silva-Filho AL, Fonseca AMRM, Santos A, Santos L, Mascarenhas T, Jorge RMN, Ferreira AM. Strength of round and uterosacral ligaments: a biomechanical study. Arch Gynecol Obstet 2013;287:313–18. doi:10.1007/s00404-012-2564-3.
[13] Resnick NM, Griffiths DJ. Expanding treatment options for stress urinary incontinence in women. JAMA 2003;290:395–7. doi:10.1001/jama.290.3.395.
[14] Cannon TW, Sweeney DD, Conway DA, Kamo I, Yoshimura N, Sacks M, et al. A tissue-engineered suburethral sling in an animal model of stress urinary incontinence. BJU Int 2005;96:664–9. doi:10.1111/j.1464-410X.2005.05702.x.
[15] Siegel AL, Kim M, Goldstein M, Levey S, Ilbeigi P. High incidence of vaginal mesh extrusion using the intravaginal slingplasty sling. J Urol 2005;174:1308–11. doi:10.1097/01.ju.0000173927.74235.e9.
[16] Wohlrab KJ, Erekson EA, Myers DL. Postoperative erosions of the Mersilene suburethral sling mesh for antiincontinence surgery. Int Urogynecol J Pelvic Floor Dysfunct 2009;20:417–20. doi:10.1007/s00192-008-0787-4.

[17] Ala-Nissila S, Haarala M, Makinen J. Tension-free vaginal tape - a suitable procedure for patients with recurrent stress urinary incontinence. Acta Obstet Gynecol Scand 2010;89:210–16. doi:10.3109/00016340903508635.

[18] Chen CC, Ridgeway B, Paraiso MF. Biologic grafts and synthetic meshes in pelvic reconstructive surgery. Clin Obstet Gynecol 2007;50:383–411. doi:10.1097/GRF.0b013e31804b184c.

[19] Kovac SR, Zimmerman CW. Advances in reconstructive vaginal surgery. Philadelphia, Pa: Lippincott Williams & Wilkins; 2007.

[20] Clemens JQ, DeLancey JO, Faerber GJ, Westney OL, McGuire EJ. Urinary tract erosions after synthetic pubovaginal slings: diagnosis and management strategy. Urology 2000;56:589–94. doi:10.1016/S0090-4295(00)00740-8.

[21] Domingo S, Alama P, Ruiz N, Perales A, Pellicer A. Diagnosis, management and prognosis of vaginal erosion after transobturator suburethral tape procedure using a nonwoven thermally bonded polypropylene mesh. J Urol 2005;173:1627–30. doi:10.1097/01.ju.0000154941.24547.0f.

[22] Kobashi KC, Dmochowski R, Mee SL, Mostwin J, Nitti VW, Zimmern PE, Leach GE. Erosion of woven polyester pubovaginal sling. J Urol. 1999;162:2070–2.

[23] US Food and Drug Administration (2008) FDA public health notification: serious complications associated with transvaginal placement of surgical mesh in repair of pelvic organ prolapse and stress urinary incontinence. Issued: October 20, 2008. Available at https://www.govinfo.gov/content/pkg/USCOURTS-ca4-15-01454/pdf/USCOURTS-ca4-15-01454-1.pdf.

[24] NIH. http://grants.nih.gov/grants/guide/rfa-files/RFA-HD-99-003.html; 1999 [accessed on 17 January 2017].

[25] Ostergard DR. Polypropylene vaginal mesh grafts in gynecology. Obstet Gynecol 2010;116:962–6. doi:10.1016/j.jmig.2010.12.012.

[26] Callister WD. Materials science and Engineering: an introduction. 4th ed. Hoboken, New Jersey: John Wiley & Sons Inc; 1996.

[27] Landau LD, Lifshitz EM. Theory of elasticity. Oxford, UK: Butterworth-Heinemann; 1986.

[28] Tirumkudulu MS, Russel WB. Cracking in drying latex films. Langmuir 2005;21:4938–48. doi:10.1021/la048298k.

[29] Xia ZC, Hutchinson JW. Crack patterns in thin films. J Mech Phys Solids 2000;48:1107–31. doi:10.1016/S0022-5096(99)00081-2.

[30] Pease LF III. Pattern formation in polymer via electrohydrodynamic instabilities and glassy fracture. Princeton, N. J.: Princeton University; 2005.

[31] Deen WM. Analysis of transport phenomena. Oxford, UK: Oxford University Press; 1998.

[32] Ho S, Suo Z. Tunneling cracks in constrained layers. J Appl Mech 1993;60:890–4. doi:10.1115/1.2900998.

[33] Brandrup J, Immergut EH. Polymer handbook. New York: Wiley; 1989.

[34] Shenoy V, Sharma A. Surface instability of soft films with coupled tension-shear interactions. J Appl Phys 2003;94:6376–85. doi:10.1063/1.1618938.

[35] Kinlock AJ, Young RJ. Fracture behavior of polymers. London: Applied Science Publishers; 1983.

[36] Strobl GR. The physics of Polymers: concepts for understanding their structures and behavior. New York: Springer; 1996.

[37] Shek KL, Dietz HP. Images of slings and meshes. Australas J Ultrasound Med 2014;17:61–71. doi:10.1002/j.2205-0140.2014.tb00108.x.

[38] Grinnell F. Fibroblast biology in three-dimensional collagen matrices. Trends in Cell Biol. 2003;13:264–9. doi:10.1016/S0962-8924(03)00057-6.